Time-Resolved Imaging of Primary Atomization Region of an Air Assist Atomizer Using an Event-Based Camera

K. Rajamanickam[1, *], Y. Hardalupas[1]

1: Dept. of Mechanical Engineering, Imperial College London, United Kingdom
* Correspondent author: k.rajamanickam@imperial.ac.uk

Keywords: Event Camera, High-Speed Imaging, Multiphase Flows, Primary Atomization, Spray Imaging

ABSTRACT

The current work discusses the demonstration of a low-cost event-based camera for time-resolved imaging (10000 frames/sec) of a primary atomization zone in canonical air-assist atomizers. Experiments have been conducted simultaneously with traditional high-speed and event-based cameras, enabling us to quantitatively assess the potential of event-based cameras in spray imaging applications. Three atomization breakup regimes are considered: columnar, bag, and multimode. Dynamic Mode Decomposition (DMD) is implemented over the instantaneous data sets acquired from both cameras to assess their performance in extracting turbulence statistics. The obtained DMD modes from both cameras are similar, highlighting the potential of low-cost event-based cameras in extracting coherent structures and their spectral contents. Finally, the limitations (e.g., event saturation) of event-based cameras in the context of primary atomization imaging are also discussed.

1. Introduction

Time-resolved imaging becomes crucial in resolving turbulence quantities whose time scales are in the order of milliseconds. In particular, such measurements are necessary for quantitatively understanding the spray formation process, where the gas-liquid phase involves complex interactions between the eddies of multiple lengths and time scales (Lasheras and Hopfinger, 2000) (Marmottant and Villermaux, 2004). Advancements in digital camera sensor technology enable the imaging of flows at high frame rates (e.g., time-resolved PIV). However, massive data storage requirements remain a bottleneck, especially for 3D imaging requiring multiple cameras. This motivates the development of alternate time-resolved imaging devices.

Event-based (EB) cameras are emerging as an alternative approach to high-speed cameras in many applications (Rebecq et al., 2019) (Gallego et al., 2020). Unlike traditional frame-based cameras, event cameras record only changes in light intensity. Each pixel on the event camera detector responds individually to contract changes, continuously producing an asynchronous stream of events. Moreover, the intensity changes are recorded in the form of binary numbers: 1 (increasing light intensity) and 0 (decreasing light intensity), significantly reducing the data size compared to the conventional high-speed cameras.

The first demonstration of an EB camera in fluid dynamics application was done by (Drazen et al., 2011). Their work showcased time-resolved particle tracking velocimetry (PTV) using an EB camera and continuous wave (CW) laser. Later, (Ni et al., 2012) and (Howell et al., 2020) demonstrated the micro PTV in channel flows. (Borer et al., 2017) employed three EB cameras to reconstruct the three-dimensional motion of helium soap bubbles in the long channel. More recently (Willert and Klinner, 2022) (Willert, 2023) showed the various potentials and limitations of EB camera PIV by comparing its results with the traditional PIV. The present work assesses event-based cameras for high-speed imaging of the primary atomization zone in canonical air-assist atomizers.

2. Coaxial and crossflow air-assist atomizer test facility

The schematic of the canonical air-assist atomizer test facility used in the present study is shown in **Figure. 1**.

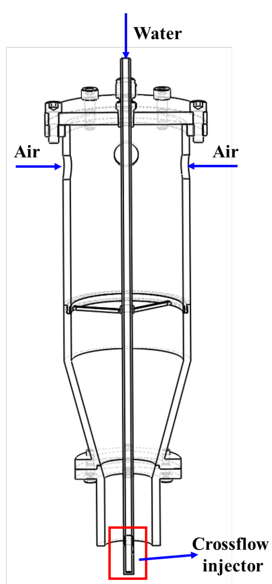

Table 1. Test conditions

Test case	Liquid Reynolds number (Re_L)	Airflow Reynolds number (Re_G)	Breakup regime
Coaxial air-assist atomizer			
A	1431	48095	Column
B	1431	47355	Bag
C	1431	54120	Multimode
Crossflow atomizer			
D	2385	53644	Column
E	2385	52429	Bag
F	2385	57503	Multimode

Figure. 1. Schematic of coaxial / crossflow atomizer

The liquid is supplied through a straight concentric tube (ID - 5mm; OD -8 mm) at the top, and the other end is connected to a removable crossflow injector. More details on the atomizer facility can be found in (Charalampous et al., 2012). The crossflow injector was closed at the end and had a circular orifice of 1mm drilled perpendicularly to its centerline. This arrangement injects the liquid jet horizontally into the incoming airflow. The same test facility, with the crossflow nozzle removed, acted as a coaxial air-assist atomizer, where the liquid was injected parallel to the airflow. During

both the crossflow and coaxial operation experiments were carried out with three different gas-phase Reynolds numbers (Re_G) representing column/oscillating, bag, and multimodal breakup regimes (**Table 1**). The liquid flow rate remains constant across all the test conditions.

3. Event-based Imaging

The simplified view of the event camera's pixel architecture and its operation is illustrated in **Figure. 2**a. Unlike frame-based cameras, each pixel in the event camera responds individually to the local luminescence changes. Each pixel in the event camera comprises a photoreceptor, differential circuit (contrast detector), and logical unit. First, the photocurrent generated by induced photons at the pixel is converted into the voltage. Then, the logarithm of the voltage is fed into the differential circuit to detect the contrast changes. Finally, the logical unit differentiates the detected contrast changes into positive (ON) and negative (OFF) events based on the light intensity. As shown in **Figure. 2**b, positive and negative events represent the change in light intensity from darker to brighter and brighter to darker, respectively.

Figure. 2 b compares the output of the spinning disc with the dot captured with frame and event-based cameras. The frame camera captures the entire disc and generates an image at a fixed sampling rate. On the other hand, the event camera continuously scans the incident light and generates the event only when the photocurrent $I(t)$ induced by the incident photons exceeds (usually >10 %) the reference threshold I_{ref} in the contrast detector. It should be noted that I_{ref} can be user-defined in most event cameras. In the example below, as the disc rotates, the light intensity changes whenever the dot traverses the pixels; hence, the event camera captures only the dot's motion. Moreover, the output from the event camera is continuous in time. The event camera stops generating the events when the disc stops, while the frame camera continues to capture the images (see **Figure. 2**c). In other words, an event camera captures only the objects moving in the scene. This is an incredibly beneficial feature in fluid flow imaging, especially near-wall flows, where the reflections/glare from the wall significantly affect the SNR. The output data stream of the event camera is in the format of $[x_i, y_i, t_i, p_i]$ where x_i, y_i representing spatial coordinates, t_i, p_i indicating the time stamp and polarity ($+1 \rightarrow ON$; $-1 \rightarrow OFF$) of the events. The image reconstruction is done by accumulating the recorded events over the specified time period. For instance, accumulating events over 1 ms generates a new image for every 1/1000s.

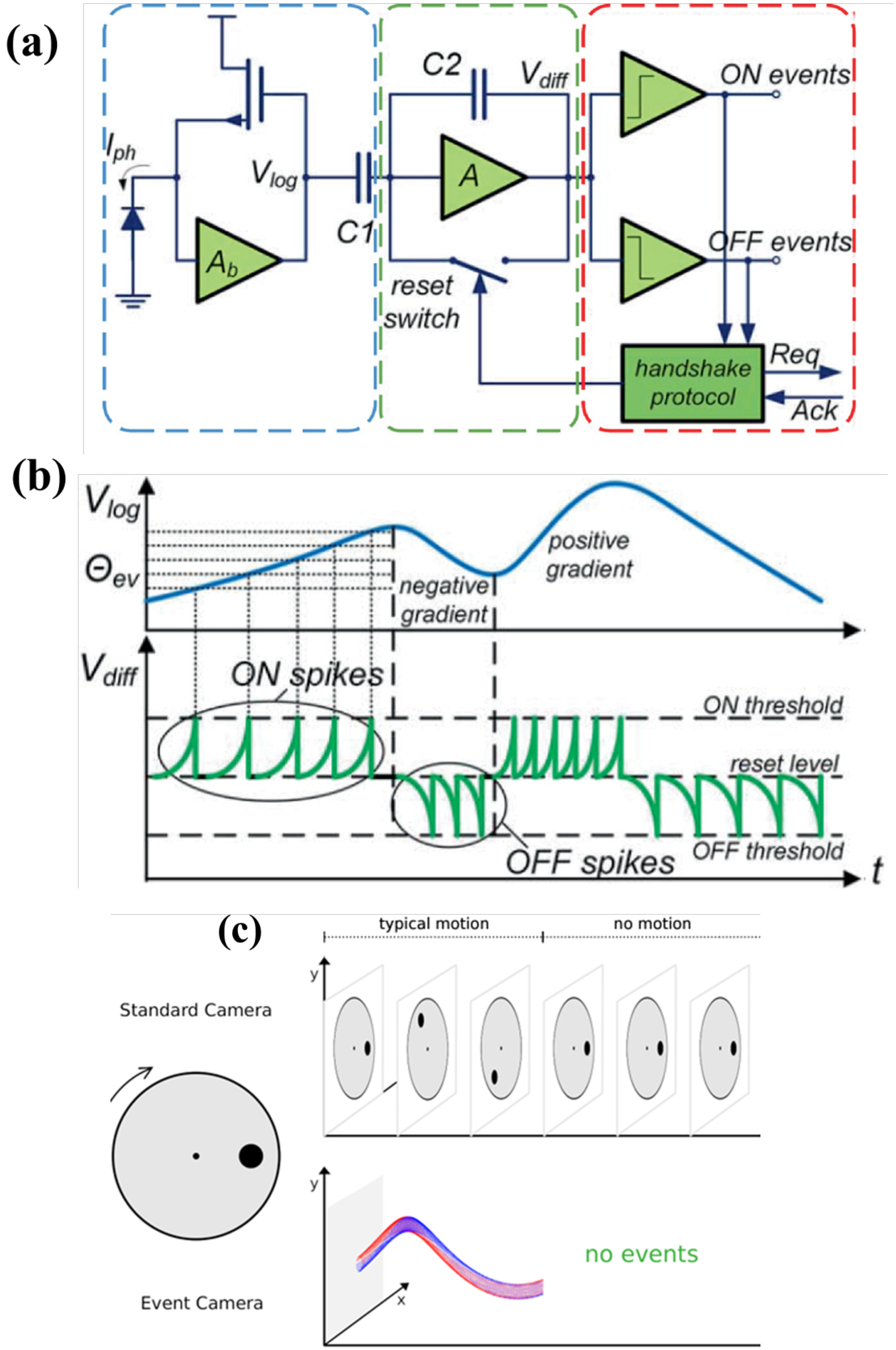

Figure. 2 a. Pixel architecture of event camera; b. working principle of contrast detector (Shao et al., 2023); c. comparison between event and frame camera (Bull and Zhang, 2021)

3.1 Time-resolved Event-based Imaging of Liquid Jet Breakup

The optical arrangement involved in the backlight imaging of a liquid jet using an event and high-speed camera is schematically illustrated in Figure. 4. DC-operated continuous wave (CW) white LED light is used for the illumination. In the present work, synchronized measurements were performed with both cameras, allowing us to assess the event camera quantitatively. A harting 10-pin network cable (09451819002XL) is customized to synchronize both cameras. The event camera (Prophsee - EVK 4; 1980 x 720 pixels) is fitted with a Nikon 50 mm lens (Aperture f/5.6), while the high-speed camera (Photron SAZ) is fitted with a Sigma 105 mm lens (Aperture f/5.6). The field of view for high-speed and event cameras is chosen as 60 mm x 60 mm (MF -136 pixels/mm) and 70 x 40 mm (MF -191 pixels/mm), respectively.

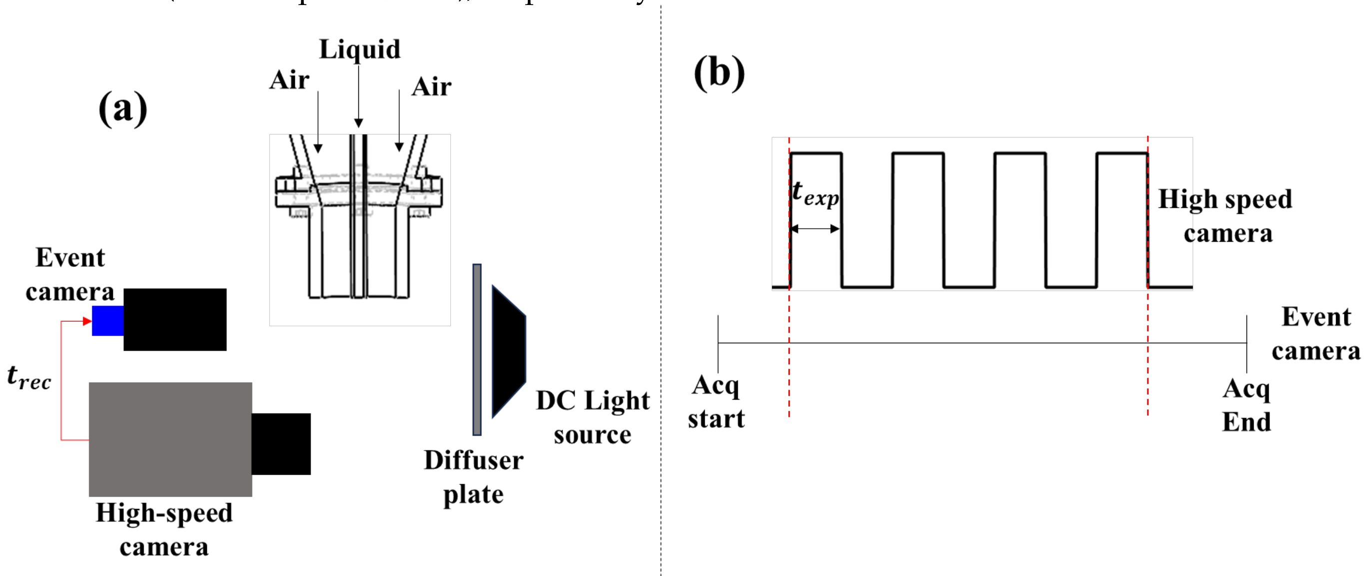

Figure. 3 a. Schematic illustrating the synchronized imaging of primary atomization using high-speed and event cameras; b. Timing diagram of high-speed and event-based cameras.

The image acquisition rate of a high-speed camera is set at 10000 fps with an exposure time of 100 µs. A total of 9700 images corresponding to the sampling time of 0.97 seconds are acquired. As illustrated in the timing diagram (**Figure. 3**b), data acquisition on the event camera started a few milliseconds earlier and stopped after a few milliseconds. Approximately 30 million events over a time period of 1.2 seconds are acquired for each case. The high-speed camera's recording time cycle (t_{rec}) is fed into the event camera output data stream $[x_i, y_i, t_i, p_i, t_{rec}]$ in the form of 1's and 0's, where '1' and '0' correspond to the ON and OFF cycles of the high-speed camera's recording sequence. This information allowed us to temporally map the event data stream with the images acquired from the high-speed camera. Finally, the event data stream is summed every 100 µs to reconstruct a total of 9700 images corresponding to 0.97 seconds. Noteworthy is that the generated events are instantly stored in the computer instead of in the imaging device's RAM (e.g., a high-speed camera). This feature of the event camera enables real-time high-speed spray imaging.

4. Results

Figure. 4 compares the images acquired simultaneously from the event and high-speed camera during columnar breakup regime operation (test cases A, D). It is worth noting that the metallic part of the atomizer exit (marked with a green box) is not visible in the images reconstructed from the EB camera. As the metallic part remains static, inducing no contrast changes, thus, no events are generated in that region. Interestingly, only a few events are witnessed in some regions of the liquid jet despite not being stationary. For instance, the captured events are sparse in the near field of the liquid jet (see areas marked with a pink box in **Figure. 3**). In contrast, many events are captured in the far field of the liquid jet (see red box). The reason is that during the columnar breakup operation, the liquid jet's interface is relatively stable in the near field, leading to the least changes in the light intensity detected by the event camera pixels at successive times. Consequently, less number of events are generated in that region. On the other hand, the liquid jet's interface undergoes strong deformation in the far field due to the instability, resulting in the detection of strong temporally varying light intensity (contrast changes) on the event camera pixels. This essentially leads to more events generated in the region where the liquid jet exhibits strong temporal oscillations.

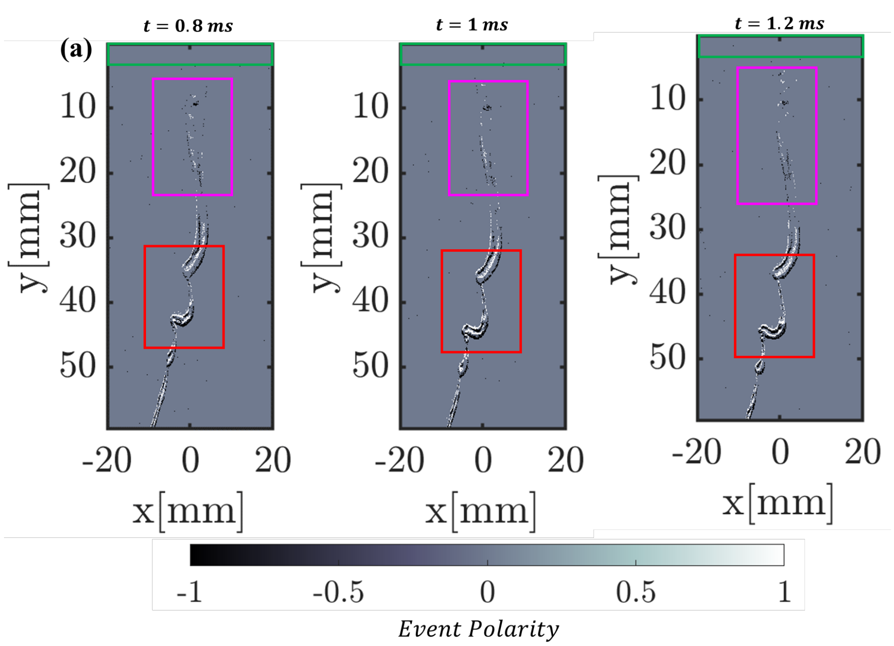

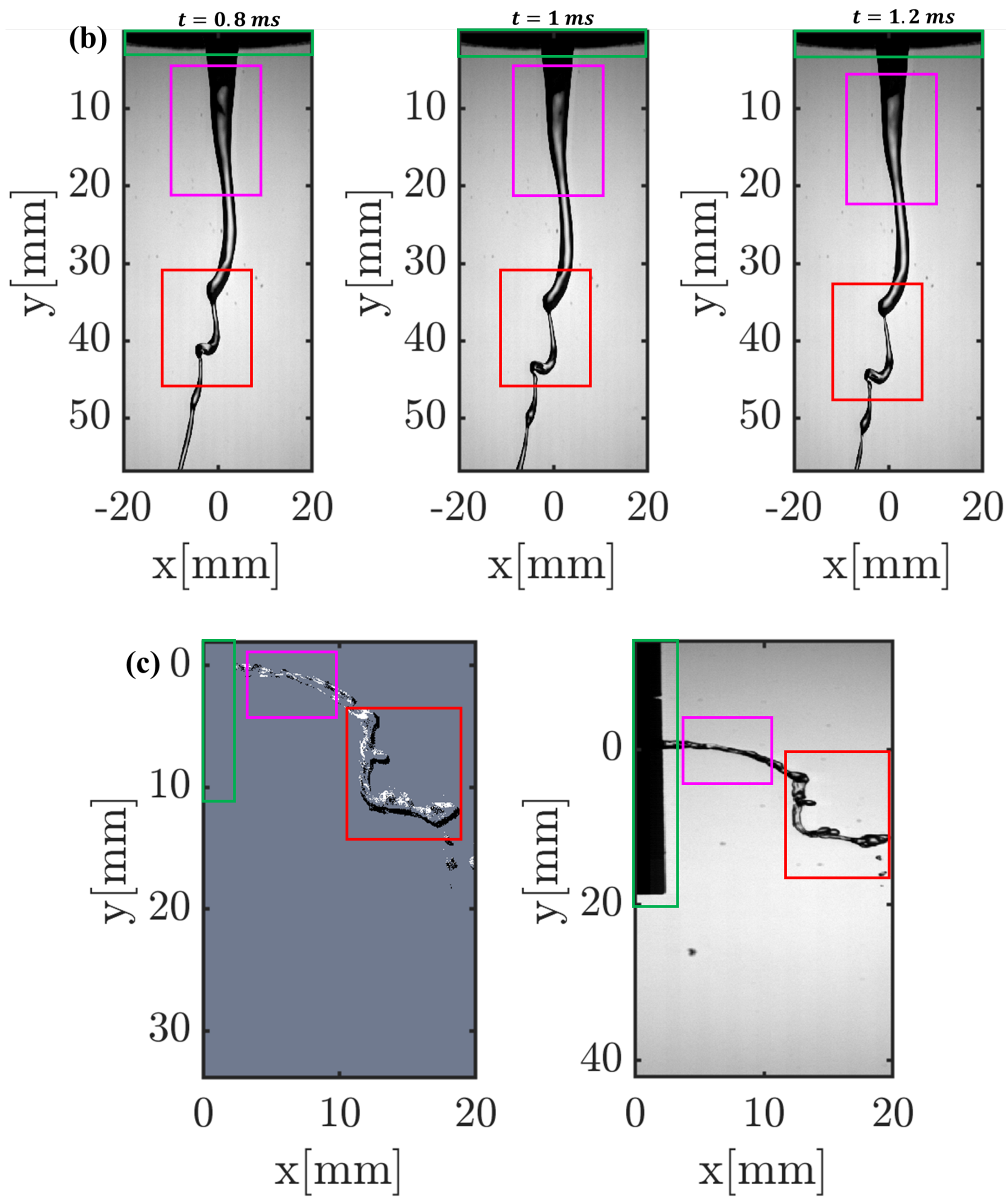

Figure. 4 Comparison of the reconstructed instantaneous image from the event camera with the images acquired from a high-speed camera

It is worth mentioning that the contrast detector threshold can be user-defined to tune the pixels' response to the light intensity / contrast changes. For example, setting the higher threshold values generates events only in regions with prominent surface deformations. This feature of the event camera is highly beneficial in computing interfacial velocities of the wavy structures on liquid jets without interference from the unwrinkled surface (e.g., regions marked with a pink box in **Figure. 4**) using algorithms like optical flow velocimetry.

Moreover, as each pixel in the event camera operates individually, the temporally varying liquid jet structures lead to dynamic changes in the event generation rate. Therefore, the file size of each reconstructed image from event data differs during the same operating condition, thus lessening data storage requirements. The two instantaneous sequences acquired during the bag breakup regime (test case B) operating condition (see **Figure. 5**) demarcate this phenomenon.

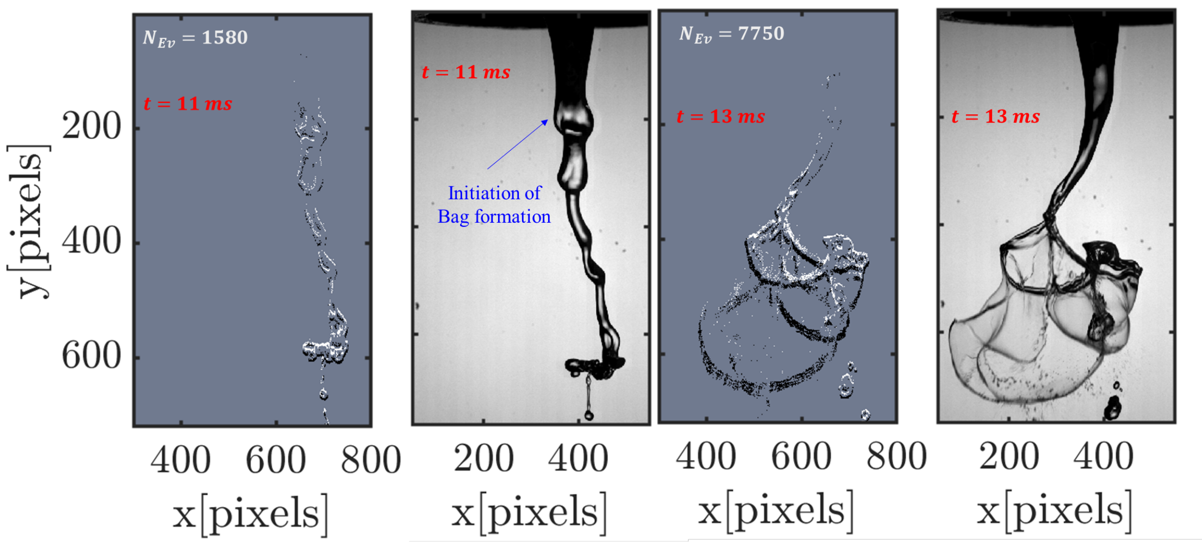

Figure. 5 Instantaneous illustration of the dynamic change in the number of events (N_{Ev}) with temporal change in the liquid jet structures.

A total of 1580 events are generated over the accumulation period of 100 microseconds in the sequence obtained before the bag breakup (**Figure. 5**; t = 11ms). On the other hand, the bag formation (**Figure. 5**; t=13 ms) on the liquid jet surface occupies many pixels (approximately 300 x 300 pixels) on the event camera, yielding 7750 events during the same accumulation period of 100 microseconds. Such dynamic switching in the event generation rate in relation to the temporally varying structures in the scene essentially reduces the memory requirements for storing the large volume of time-resolved data.

5. Comparison of coherent structures

Dynamic Mode Decomposition (DMD) has been applied to the instantaneous data sets of high-speed and event cameras to compare their performance in capturing coherent structures. For brevity, only the results corresponding to the columnar /wavy breakup regime of a crossflow atomizer (test case D; **Table 1**) are shown.

For the DMD implementation, first, the data matrix $\boldsymbol{X}(\boldsymbol{x_1}, \boldsymbol{x_2}, \ldots \boldsymbol{x_m})$ is converted into two time-shifted data sets $\boldsymbol{X_1}(\boldsymbol{x_1}, \boldsymbol{x_2}, \ldots \boldsymbol{x_{m-1}})$ and $\boldsymbol{X_2}(\boldsymbol{x_2}, \boldsymbol{x_2}, \ldots \boldsymbol{x_m})$. Next, the linear operator $\boldsymbol{A}$ can be obtained by taking the pseudo inverse of $\boldsymbol{X_1}$ **and** $\boldsymbol{X_2}$ as follows,

$$A\boldsymbol{X_1} = \boldsymbol{X_2} \tag{1}$$

$$A = \boldsymbol{X_2}\boldsymbol{X_1^{\dagger}} \tag{2}$$

As the data matrix ($\boldsymbol{X}$) size is too large, singular value decomposition (SVD) is necessary to find the best fit for the linear operator. Furthermore, optimal rank $\boldsymbol{r}$ obtained based on the higher order modes is used for truncation. The pseudo-inverse matrix can be written as:

$$\boldsymbol{A} = \boldsymbol{X_2}\boldsymbol{\Sigma}^{-1}\boldsymbol{X}_1^{\dagger}\boldsymbol{U}^{*} \tag{3}$$

The projection of full matrix A on the POD modes yields the linear operator $\widetilde{\boldsymbol{A}}$

$$\widetilde{\boldsymbol{A}} = \boldsymbol{U}^{*}\boldsymbol{A}\boldsymbol{U} \tag{4}$$

$$\widetilde{\boldsymbol{A}} = \boldsymbol{U}^{*}\boldsymbol{X_2}\boldsymbol{V}\boldsymbol{\Sigma}^{-1}$$

The eigenmode decomposition of $\tilde{A}$ yields eigenvectors $\boldsymbol{W}$ and eigenvalues $\boldsymbol{\lambda}$

The corresponding eigenmodes can be computed by projecting the eigenvectors $\boldsymbol{W}$ onto $\boldsymbol{U}$:

$$\boldsymbol{\Phi} = \boldsymbol{U}\boldsymbol{W} \tag{5}$$

where the frequencies ($\boldsymbol{f_i}$) and growth rates ($\boldsymbol{\sigma_i}$) can be computed from the eigenvalues

$$\boldsymbol{f_i} = \mathrm{Im}\left(\frac{log\lambda_j}{2\pi\Delta t}\right) \tag{6}$$

$$\boldsymbol{\sigma_i} = \mathbf{Re}\left(\frac{log\lambda_j}{2\pi\Delta t}\right) \tag{7}$$

Finally, the modal amplitudes ($\boldsymbol{C}$) are obtained from the pseudo inverse of the DMD mode ($\boldsymbol{\Phi}$) and initial snapshot:

$$\boldsymbol{C} = \boldsymbol{\Phi}^{\dagger}\boldsymbol{x_1} \tag{8}$$

The DMD frequency spectrum obtained by applying the optimal rank $\boldsymbol{r}$ is illustrated in **Figure.** 7, and the frequencies corresponding to the first four modal amplitudes are marked. The frequencies of the first four modes are approximately the same between both the cameras, except that some higher order frequencies around 3000 - 4000 Hz are noticed in the event camera's DMD spectrum (**Figure.** 7b). These broad-band frequencies might have originated due to the noise in the detectors.

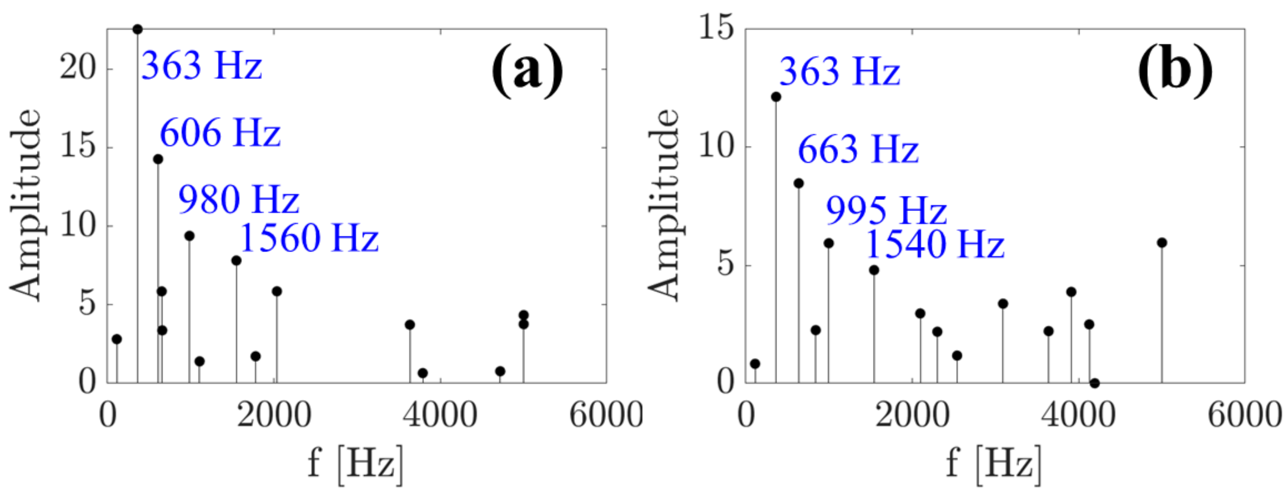

Figure. 6 DMD spectrum a. High-speed camera; b. Event camera.

The spatial structures corresponding to the first four DMD modes are illustrated in **Figure. 8**. Interestingly, both cameras represent similar modal features. For example, the first two modes (M1-M2) represent the large-scale oscillation (also known as flapping mode) of the liquid jet around the mean trajectory. The wave-like structure obtained in modes 3- 4 indicates the wave-induced breakup of the liquid jet in the downstream region.

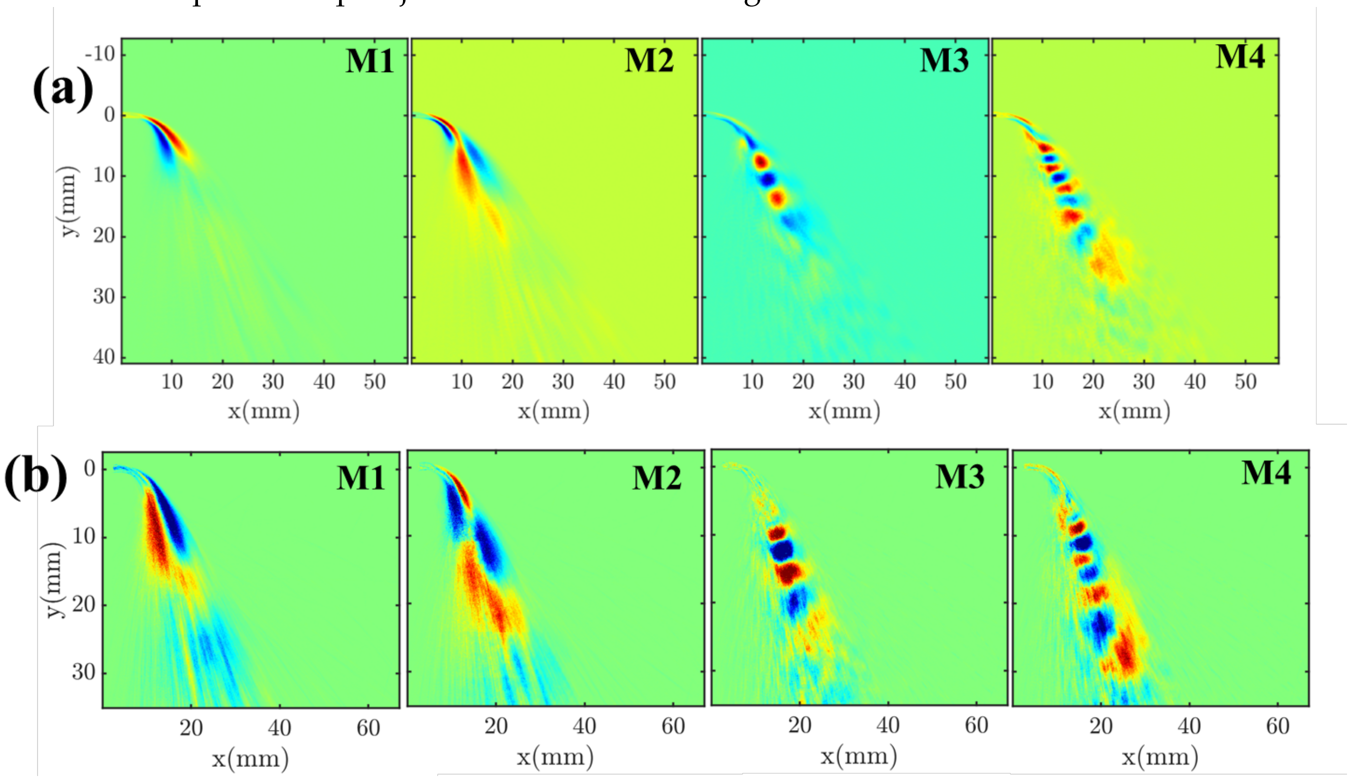

Figure. 7 Comparison of dominant DMD spatial modes obtained from a. high-speed camera; b. event-based camera.

6. Limitations of Event-based imaging in spray applications

Previous studies (Wang et al., 2020) (Willert and Klinner, 2022) have reported the event saturation/pixel latency issue in applications that involve too many events (e.g., dense PIV particles). Magnified imaging of the bag breakup regime with a field of view of 20 x 15 mm (MF - 64 pixels/mm) is performed to assess this phenomenon in spray applications. The time sequence of the single-bag breakup event obtained with magnified viewing is illustrated in **Figure. 8.** Approximately 80% of the pixels are exposed when capturing the bag breakup at a high magnification ratio, resulting in a three-fold increase in the total number of events per unit time. Consequently, event saturation is witnessed in the successive images (marked with arrows; **Figure. 8**). Following the event saturation, the detector no longer reacts promptly to the contrast changes in the scene. This introduces a delay of several microseconds between the time assigned to the events and the real-time of the actual event occurrence. The images captured simultaneously with the high-speed camera confirmed this; for example, the actual time instant of the below sequence is 1000 μs earlier than the time stamps assigned in the event data stream. Another significant drawback of the event camera is that it cannot measure the absolute light intensity, limiting its application in fluorescence imaging (e.g. LIF).

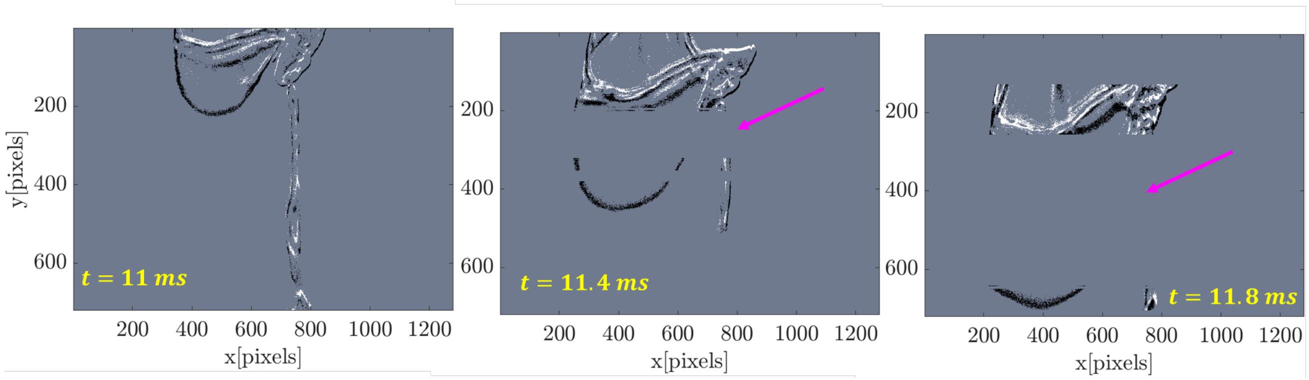

Figure. 8 Sequences illustrating the event saturation phenomenon observed during high magnification imaging of the bag breakup process.

4. Conclusions

The present work demonstrates an alternative approach to high-speed imaging using a low-cost event-based camera. The application is focused on the time-resolved (10000 frames/sec) shadow imaging of the primary atomization zone in the canonical air-assist atomizers. Synchronized experiments have been conducted to assess both cameras' performance quantitatively. The instantaneous images reconstructed from the event camera are comparable to the ones acquired with the high-speed camera. Subsequently, DMD is implemented to compare the coherent structures obtained from both cameras. The obtained DMD modes from both cameras are similar, highlighting the potential of low-cost event-based cameras in extracting coherent structures and their spectral contents.

Acknowledgments

The authors would like to acknowledge the funding support from the Engineering and Physical Sciences Research Council (EPSRC) through the UKRI Horizon Europe Guarantee award scheme- grant no- EP/X026248/1 (originally awarded as Marie Curie Individual Fellowship).

References

Borer, D., Delbruck, T., Rösgen, T., 2017. Three-dimensional particle tracking velocimetry using dynamic vision sensors. Exp. Fluids 58, 165.

Bull, D., Zhang, F., 2021. Intelligent image and video compression: communicating pictures. Academic Press.

Charalampous, G., Hadjiyiannis, C., Hardalupas, Y., 2012. Numerical and experimental investigation of the optical connectivity technique in cross flow atomization, in: 12th International Conference on Liquid Atomization and Spray Systems, Heidelberg, Germany.

Drazen, D., Lichtsteiner, P., Häfliger, P., Delbrück, T., Jensen, A., 2011. Toward real-time particle tracking using an event-based dynamic vision sensor. Exp. Fluids 51, 1465–1469. h

Gallego, G., Delbrück, T., Orchard, G., Bartolozzi, C., Taba, B., Censi, A., Leutenegger, S., Davison, A.J., Conradt, J., Daniilidis, K., 2020. Event-based vision: A survey. IEEE Trans. Pattern Anal. Mach. Intell. 44, 154–180.

Howell, J., Hammarton, T.C., Altmann, Y., Jimenez, M., 2020. High-speed particle detection and tracking in microfluidic devices using event-based sensing. Lab. Chip 20, 3024–3035.

Lasheras, J.C., Hopfinger, E.J., 2000. Liquid Jet Instability and Atomization in a Coaxial Gas Stream. Annu. Rev. Fluid Mech. 32, 275–308.

Marmottant, P., Villermaux, E., 2004. On spray formation. J. Fluid Mech. 498, 73–111.

Ni, Z., Pacoret, C., Benosman, R., Ieng, S., Régnier*, S., 2012. Asynchronous event-based high speed vision for microparticle tracking. J. Microsc. 245, 236–244.

Rebecq, H., Ranftl, R., Koltun, V., Scaramuzza, D., 2019. High speed and high dynamic range video with an event camera. IEEE Trans. Pattern Anal. Mach. Intell. 43, 1964–1980.

Shao, B., Wang, Y., Cai, Z., Zhao, J., 2023. Event Camera Visualization, in: Yan, L., Duan, H., Deng, Y. (Eds.), Advances in Guidance, Navigation and Control, Lecture Notes in Electrical Engineering. Springer Nature Singapore, Singapore, pp. 6023–6032.

Wang, Y., Idoughi, R., Heidrich, W., 2020. Stereo Event-Based Particle Tracking Velocimetry for 3D Fluid Flow Reconstruction, in: Vedaldi, A., Bischof, H., Brox, T., Frahm, J.-M. (Eds.), Computer Vision – ECCV 2020, Lecture Notes in Computer Science. Springer International Publishing, Cham, pp. 36–53.

Willert, C.E., 2023. Event-based imaging velocimetry using pulsed illumination. Exp. Fluids 64, 98.

Willert, C.E., Klinner, J., 2022. Event-based imaging velocimetry: an assessment of event-based cameras for the measurement of fluid flows. Exp. Fluids 63, 101.